AFRL-AFOSR-JP-TR-2021-0001

Enabling quantum information technology with 60 photons and beyond

Ralph, Timothy
QUEENSLAND UNIVERSITY OF TECHNOLOGY
2 GEORGE ST
BRISBANE, , 4000
AUS

07/25/2021
Final Technical Report

Air Force Research Laboratory
Air Force Office of Scientific Research
Asian Office of Aerospace Research and Development
Unit 45002, APO AP 96338-5002

REPORT DOCUMENTATION PAGE

Form Approved
OMB No. 0704-0188

1. REPORT DATE *(DD-MM-YYYY)*
25-07-2021

2. REPORT TYPE
Final

3. DATES COVERED *(From - To)*
15 Apr 2019 - 14 Apr 2021

4. TITLE AND SUBTITLE
Enabling quantum information technology with 60 photons and beyond

5a. CONTRACT NUMBER
FA2386-19-1-4043

5b. GRANT NUMBER

5c. PROGRAM ELEMENT NUMBER
61102F

6. AUTHOR(S)
Timothy Ralph

5d. PROJECT NUMBER

5e. TASK NUMBER

5f. WORK UNIT NUMBER

7. PERFORMING ORGANIZATION NAME(S) AND ADDRESS(ES)
QUEENSLAND UNIVERSITY OF TECHNOLOGY
2 GEORGE ST
BRISBANE, 4000
AUS

8. PERFORMING ORGANIZATION REPORT NUMBER

9. SPONSORING/MONITORING AGENCY NAME(S) AND ADDRESS(ES)
AOARD
UNIT 45002
APO AP 96338-5002

10. SPONSOR/MONITOR'S ACRONYM(S)
AFRL/AFOSR IOA

11. SPONSOR/MONITOR'S REPORT NUMBER(S)
AFRL-AFOSR-JP-TR-2021-0001

12. DISTRIBUTION/AVAILABILITY STATEMENT
A Distribution Unlimited: PB Public Release

13. SUPPLEMENTARY NOTES

14. ABSTRACT
The experimental and theoretical advances demonstrate the viability and potential of multiplexed photonic states for large-scale quantum tasks. The high efficiency, flux and precision switching they achieved showed that these attributes are useful for flexible and high- performance Noisy Intermediate Scale Quantum (NISQ) devices, ultimately providing a real-world system on which to develop new algorithms, tasks, and error handling protocols, with a precision and flexibility that can outperform competing technologies and demonstrations.

15. SUBJECT TERMS

16. SECURITY CLASSIFICATION OF:			17. LIMITATION OF ABSTRACT	18. NUMBER OF PAGES	19a. NAME OF RESPONSIBLE PERSON
a. REPORT	b. ABSTRACT	c. THIS PAGE			CHRISTOPHER VERGIEN
U	U	U	SAR	30	19b. TELEPHONE NUMBER *(Include area code)* 315-227-7002

Enabling quantum information technology with 60 photons and beyond

S. Slussarenko, A. P. Lund, G. J. Pryde, T. C. Ralph

14 April 2020

Contents

Glossary

FWHM	full width at half maximum
HEMT	high-electron-mobility transistor
i.i.d	independent and identically distributed
JSI	joint spectral intensity
KTP	potassium titanyl phosphate
PBS	polarizing beam-splitter
PCB	printed circuit board
PMF	phase-matching function
pp-KTP	periodically-poled potassium titanyl phosphate
RLC	Resistor, Inductor, Capacitor
SNSPD	superconducting nanowire single photon detectors
SPDC	Spontaneous Parametric Downconversion
TVD	total variation distance

Symbols

$\|n\rangle$	single mode fock state with photon number n
$\|n, m\rangle$	two mode fock state with photon number n in the first mode and photon number m in the second mode
η_i	effective intensity loss of ith mode
$P(n, m)$	probability of counting n photons in the first mode and m photons in the second mode
R_L	shunt resistance
r	squeezing strength parameter
$\chi = \tanh r$	alternative squeezing strength parameter

1 Introduction

This document is the final report for the project: *Enabling quantum information technology with 60 photons and beyond*. The aim of this project was to use high-heralding-efficiency spontaneous parametric downconversion (SPDC), with fine optical mode control, and world-leading superconducting photon detectors to generate correlated states of many tens of photons in a so-called scatter-shot state across many temporal modes. When generated and detected with sufficiently high fidelity and efficiency, these states are directly useful for solving classically intractable sampling problems. They are also expected to be useful for metrology and error-corrected states for quantum communication. Further, they provide a powerful resource for building a deterministic single photon source when coupled with fast switching.

A summary of our key results are:
1. Experimental demonstration of the heralded production and characterization of over 100 photons in a time-bin scattershot state, supported by theoretical modeling;
2. Experimental demonstration of the ability to switch heralded photons between time-bin states without loss of indistinguishability;
3. Theoretical investigation of applications of scattershot sources in quantum interference and metrology.

Our experimental and theoretical advances demonstrate the viability and potential of multiplexed photonic states for large-scale quantum tasks. The high efficiency, flux and precision switching we achieved shows that these are useful for flexible and high- performance Noisey Intermediate Scale Quantum (NISQ) devices, ultimately providing a real-world system on which to develop new algorithms, tasks, and error handling protocols [1], with a precision and flexibility that can outperform competing technologies and demonstrations. The next steps are to scale up the source array, hybridise the mode manipulation scheme to combine spatial and temporal modes, and to actively phase lock the system. At the end of this document, we will provide a concrete proposal for the next steps to achieve these goals.

Our report is organized in the following way. In Section 2 we present our results on the performance and theoretical modelling of our scatter-shot source, addressing Research Element 1 of the research program. In Section 3 we present theoretical results on future applications of the scatter-shot source, addressing Research Element 5. In Section 4 we report progress towards the qualitative and quantitative advances of the scatter-shot source, including implementation of cryogenic amplifiers, tailoring the non-linearties of our source crystals and the development of a photon switching capability, addressing Research Elements 2, 3 and 4 respectively. Finally in Section 5 we summarize our results and discuss future directions.

2 Scatter-shot Photon Source

2.1 Theoretical Model

2.1.1 Overview

Scatter-shot boson sampling uses many SPDC sources producing two-mode squeezing as the fiducial resource state [2, 3], as opposed to multiple single photon Fock states [4]. Interactions

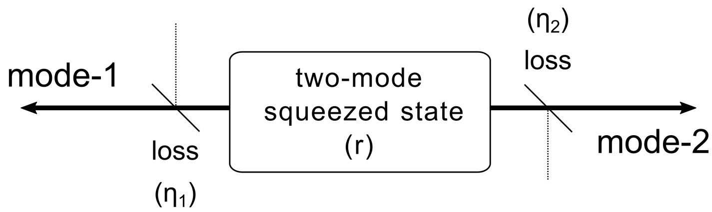

Figure 1: Schematic representing the theoretical model parameters used in estimating the performance of the source.

between the multitude of two-mode squeezed states is needed to perform computationally difficult tasks. But at the first instance, one need only consider each two-mode squeezed state as generated randomly and independently. In this instance, the most significant sources of experimental errors are expected to be due to loss, mode matching and of a lower order, thermal effects within detection.

The two-mode squeezed state is from the class of states that have Gaussian probability distribution when measured within any quadrature. This means that these three deleterious effects can be traded off between each other to model a situation covering all of these, provided one can encapsulate within the model a varied rate of squeezing and loss. For example, a completely thermal state results if one of the two modes suffers 100% loss, the temperature of which can be varied by the choice of squeezing parameter.

When coupling via single-mode fibre, mode-mismatches are effectively converted to loss. At the end of the line, this state will be detected in the number or Fock basis. In this case, if the coupling to detection is multi-mode, and each mode is detected equally (i.e. high quantum efficiency detection), then the mode mis-matches at the detector will not change the Fock basis detection result. This is because the detection cannot observe any relative coherence between mis-matched modes and mis-matched modes do not change the total amount of energy present. The quantum efficiency of the detectors can also be incorporated into the model loss.

2.1.2 Model parameters

The effective model for each two-mode squeezed state within the source is described by three parameters: two-mode squeezing (r), mode-1 loss (η_1) and mode-2 loss (η_2).

The two-mode squeezed state without losses can be written in the Fock basis

$$\sqrt{\operatorname{sech} r}\sum_{n=0}^{\infty}\tanh(r)^n\left|n,n\right\rangle ,$$

with r allowed to take values from all non-negative real numbers. It is convenient to talk about other parameterisation such as the trigonometrical removed $\chi = \tanh r$ or the practically useful and widely reported squeezing in dB $= 10r/\log_{10} e$. The resultant probability distribution in the Fock basis for detecting this state is

$$P(n_1,n_2) = \frac{\tanh^{2n} r}{\cosh r}\delta_{n_1,n_2}$$

where n_i is the photon number in the ith mode and $\delta_{n,m}$ represents the Kronecker delta which is zero except when $n = m$ and it is one. Of particular importance to the experiment here is the cases when n_1 and n_2 are either 0 or 1. These terms will dominate the individual statistics of each mode as it is the combinatorial combinations of these photons that scales up the photon source.

Incorporating losses into this distribution can be performed for the 0 and 1 by considering how many ways photons can be lost to give the particular Fock count and summing over all those possibilities. For example, in the case of $P(0,0)$:

$$P(0,0) = \operatorname{sech} r \sum_{p=0}^{\infty} (\tanh^{2p} r) \eta_1^p \eta_2^p = \operatorname{sech} r (1 - \tanh^2 r \eta_1 \eta_2)^{-1}$$

where p in the summation represents the number of photons lost in each case. For the case of zero total photons detected, the only allowed case is for all photons to be lost, hence no combinatorial factors are needed here. At this point it is easiest to work without the trigonometric parameters and use χ. The probabilities are then

$$P(0,0) = \frac{1-\chi^2}{1-\chi^2\eta_1\eta_2}$$

$$P(0,1) = \frac{(1-\eta_1)\eta_2\chi^2(1-\chi^2)}{(1-\chi^2\eta_1\eta_2)^2}$$

$$P(1,0) = \frac{\eta_1(1-\eta_2)\chi^2(1-\chi^2)}{(1-\chi^2\eta_1\eta_2)^2}$$

$$P(1,1) = \frac{(1-\eta_1)(1-\eta_2)\chi^2(1-\chi^2)}{(1-\eta_1\eta_2\chi^2)^2} + \frac{2\eta_1(1-\eta_1)\eta_2(1-\eta_2)\chi^4(1-\chi^2)}{(1-\eta_1\eta_2\chi^2)^3}$$

Whilst one can merely compute these probabilities, their form is somewhat intuitive. The denominators represent the cascading of higher order down-conversion events as they contribute to the probability due to the losses. The numerator contains terms explaining from which part of the two-mode squeezed state the terms are generated. All terms must have a $(1-\chi^2)$ for normalisation. Terms involving 1 are those whose sums start at zero, terms involving χ^2 are those where the cascade started from a pair of photons. In order to generate the $P(0,0)$ term then the cascade must start from the vacuum and hence this is the only contribution. In the $P(0,1)$ the cascade must start from a single photon pair (zero pairs cannot make any photons) and hence attracts a numerator with χ^2. However, a photon in mode 1 must be lost relative mode 2 and this gives the form $\eta_1(1-\eta_2)$. The $P(1,1)$ is the most complex here as it involves two possible cascades. The first term is a cascade from a pair of photons where both are lost. The second term involves a cascade with two pairs of photons where a single photon is lost from each. The extra 2 comes from the multiple possibilities of ways to lose these photons with the added restriction that the photons are indistinguishable.

From here on we will use these probabilities to model each temporal mode of the source. The multiple photon statistics will result from the combination of many modes with these probabilities.

2.2 Experimental Results

2.2.1 Procedure

Our key idea in experimentally generating the required fiducial resource state is to combine a single ultra-high efficiency SPDC source developed by Pryde and his team (Fig. 2(a)) with

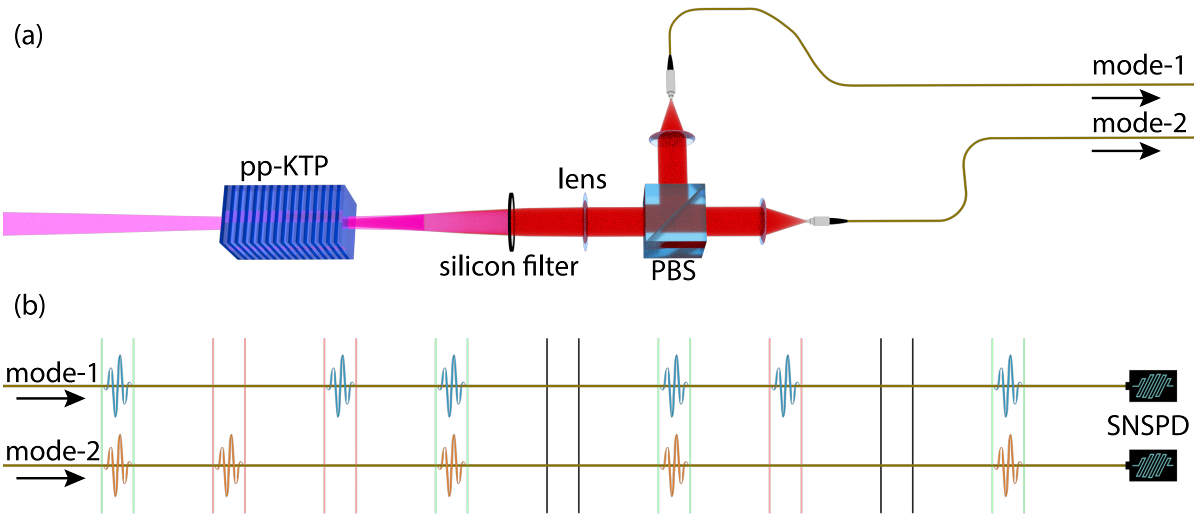

Figure 2: (a) Schematic representing the experimental setup of the scattershot source. (b) Time-mode encoding approach: black, red and green lines denote time modes that are not populated by photons, have one photon in either mode-1 or mode-2, or are both occupied by a photon, respectively.

the temporal mode allocation scheme, developed by Ralph and co-workers. In our scheme, a modelocked Ti:sapphire laser with a center wavelength of 775 nm and FWHM of 5.35 nm was used to pump a pp-KTP crystal in the collinear geometry and with type-II phasematching. The co-propagating downconverted photons were separated using a polarizing beam splitter (PBS) and the pump was blocked by a silicon filter. No spectral filtering was applied to the downconverted photons at this stage of experiment. The photons were coupled into single-mode optical fibers and were then detected using superconducting nanowire single photon detectors (SNSPD). The detection signal from SNSPDs was recorder by a time-tagging hardware, where each detection event was given an associated timestamp, with a resolution of 156.25 ps. The crucial requirement for this setup was to minimize η_1 and η_2. This consists in (a) selecting appropriate pump and collection optical modes in order to ensure that photons are generated in optical modes that have maximum compatibility with the optical fiber modes [5]; and (b) optimizing the experimental layout and fiber coupling techniques in order to minimize the fiber coupling loss due to misalignment, mode mismatch and instability. For this task, each optical fiber and fiber coupling lens were mounted on high precision mounts, with a total of 8 degrees of freedom per fiber, for fine adjustment and control. The pump power was used to adjust the squeezing parameter r, so the time-tag data was acquired for several pump powers, ranging from 25 mW to 300 mW. The acquired data was then analyzed in post-processing with the following steps.

1) Establishment of time modes. Our scheme uses two spatial modes (mode-1 and mode-2) and multiple time modes instead of spatial modes only to be populated with photons. The time modes are defined by the repetition rate of the femtosecond pump laser and are separated by ≈ 12.3ns. However, in order to analyse thousands of modes, this timing must be calculated with extreme precision: an inaccuracy of 0.1ps, for example, will give an error of 1ns already after 10000 modes, which is almost an order of magnitude larger than the pump pulse length.

Standard analysis methods proved to be insufficient, so the time mode separation time was recovered directly from the photon arrival and detection statistics.

2) Detector reset time filtering and dark counts rejection. In our current configuration, the detector recovery time is longer than the time distance between two adjacent time modes. This obstacle will be overcome using cryogenic amplification of the detector readout (see Section 4). In order to analyze the current data, several temporal modes (depending on the detector reset time) that follow any detection event on any of the photons are rejected from the data, on both mode-1 and mode-2 channels, simultaneously. Under the independent and identically distributed (i.i.d) assumption, such filtering does not affect the results of our tests. Additionally, detection events that appear outside the established time modes correspond to the dark counts of the detectors and also lead to a temporary blinding of the channel. Time modes that appear after such detection events are also rejected from the analysis.

3) The cleaned-up data is divided into segments of m modes (with m ranging from 64 to $\approx 60,000$) and the content of each segment is analyzed in terms of single (mode-1 or mode-2) and coincidence (mode-1 and mode-2) detection events, as shown in Fig. 2(b).

2.2.2 *Data and analysis*

(a)

Event	Number
$(0,0)$	99702
$(0,1)$	58
$(1,0)$	43
$(1,1)$	197

(b)

Parameter	Estimate
r	0.056 ± 0.005
η_1	0.18 ± 0.08
η_2	0.23 ± 0.08

Table 1: (a) The scattershot source event data for a run of $100\,000$ samples with temporal events grouped individually. (b) Maximum likelihood estimates for the model parameters. The r squeeze parameter here is equivalent to approximately 0.24dB. Uncertainties are formed from the Fisher information of the maximum likelihood estimation and are three standard deviations.

The theoretical model and experimental data presented are in broad agreement but differ in the detail within the distributions. The individual counting statistics from the experimental data match the i.i.d model well using the estimate of the underlying model parameters from the 1-mode data. The 1-mode model estimate has a rather large uncertainty in the parameters that is not reflected in these figures. Better estimates of the model parameters can be made up to a point, through collection of more data. However, at some stage the uncertainty will be determined by the mismatching features of the theory and experiment.

To compare the theoretical and experimental data, the total variation distance (TVD) of the counting and coincidence sub-distributions can be used to lower bound the actual TVD. The TVD is a quantity representing the probability that one would determine that two distributions are different purely through sampling their events. The TVD of two distributions is 0 if they are exactly the same. In this instance, as the number of photons counted, or the singles and coincidences counted are determined by combining many events together to produce a single data point, the TVD calculated using these distribution is a lower bound to the true TVD.

The rapid increase in TVD shown in Figure 7, as the number of modes considered increases is due here mostly to the imprecision of the underlying estimated model parameters. As the

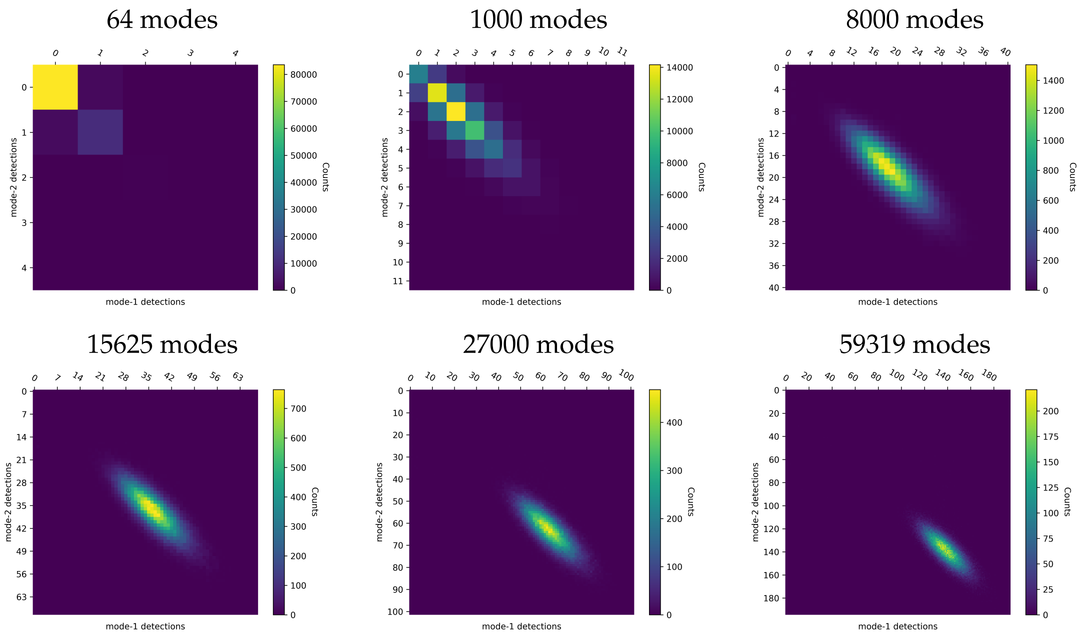

Figure 3: Post-processed experimental counts for 64, 1000, 8000, 15625, 27000 and 59319 temporal modes, with total mode-1 counts on the horizontal axis and mode-2 counts on the vertical. Each plot represents 100 000 samples. These counts do not capture coincidences between temporal modes.

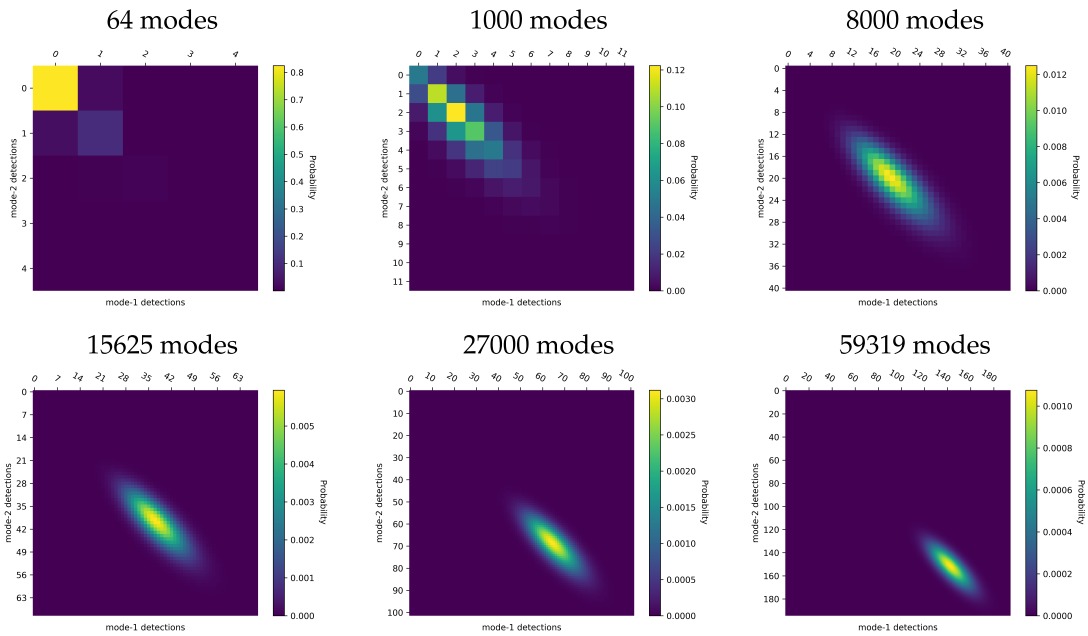

Figure 4: Theoretically modelled probabilities for i.i.d two-mode squeezing with estimated experimental parameters from Table 1.

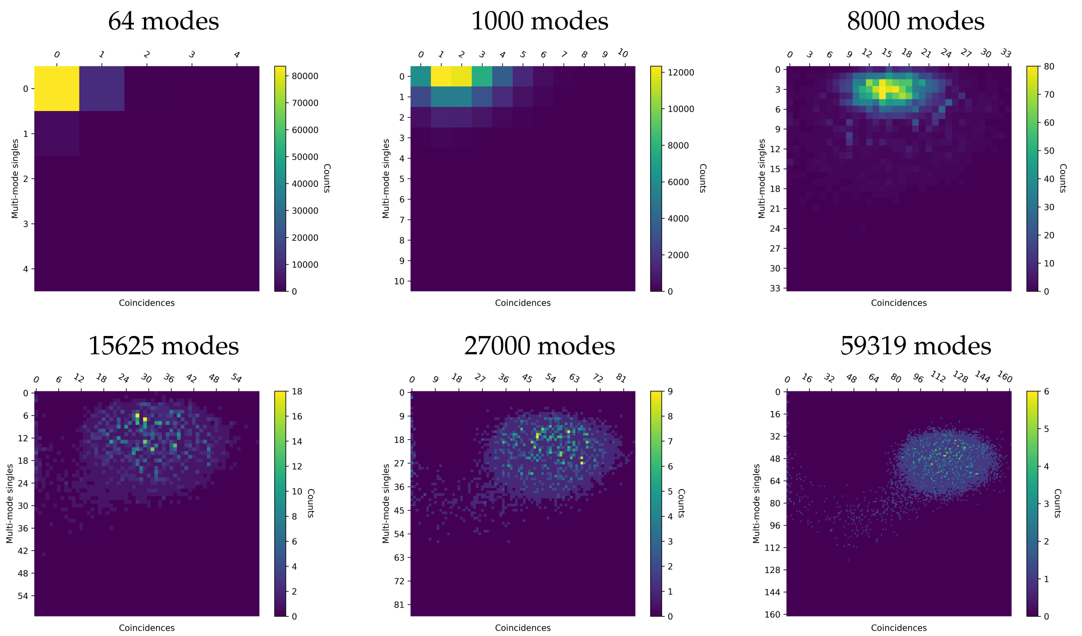

Figure 5: Experimental counts of location independent singles (excluding coincidences) vs coincidences when considering many modes. A distribution with no loss ($\eta_1 = \eta_2 = 0$) would have no singles present which would correspond to the distribution being concentrated at the top of the figure.

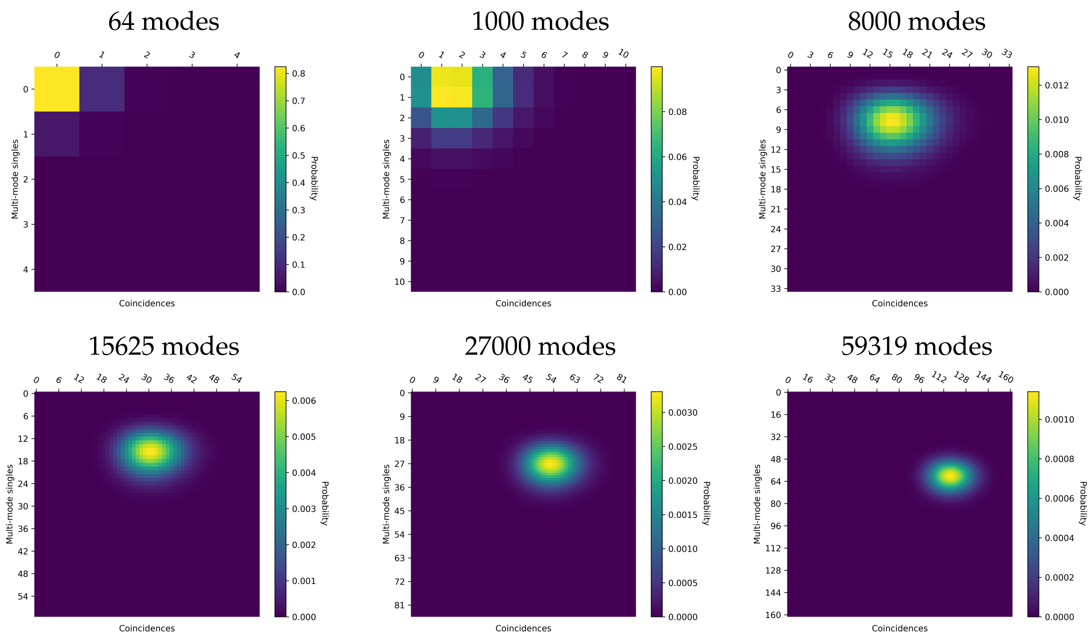

Figure 6: Theoretically modelled probabilities of singles vs coincidences for i.i.d two-mode squeezing with estimated experimental parameters from Table 1. These plots show a distribution that is generally lower on the plot than the experimental data. This suggests that the theoretically estimated loss parameters from the single-mode data is slightly over estimated.

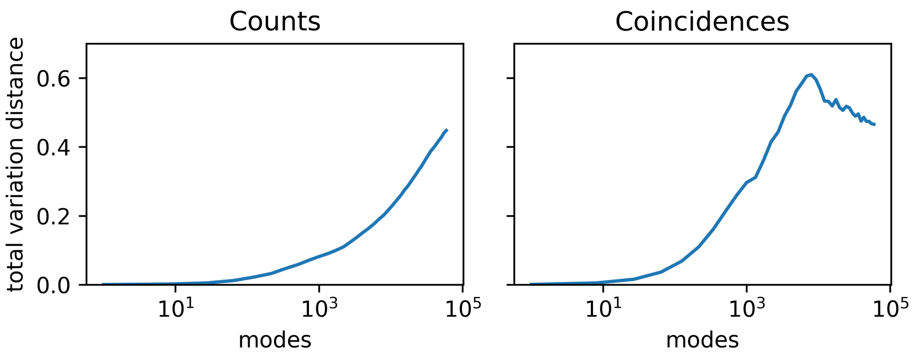

Figure 7: Total variation distance (TVD) lower bound between the theoretically modeled distribution and the experimental data. The left plot show the bound of the counting distribution and the right plot shows the bound for the distribution of coincidences and singles.

number of modes increases, the total number of events available to distinguish the distributions increases (i.e. the total number of photons). Therefore the TVD will be more sensitive to any differences in the distributions. This is particularly evidenced in the TVD for the coincidences and singles distribution. With more data these differences will be reduced.

The substructures present in the experimental data that are not present in the theoretical distribution will ultimately limit the ability of this model to represent the performance of the source. The major differences are the width of the distribution and the feint tail in the distribution when many modes are considered. These effects could have a number of sources, but are likely due to unaccounted for effective thermality, timing jitter and the performance of the post-processing filtering. Understanding these features and incorporating them into the model are the clear next steps in modelling the source.

3 Applications of Scatter-shot Source

Linear optical networks, coupled with single photon sources and detectors and feedforward, can be used for numerous quantum processing tasks right up to universal quantum computation [6]. In general the technical requirements for implementing full-scale quantum computation are extremely challenging. However, recent theoretical and experimental advances have made the possibility of implementing specific quantum processing systems on larger scales an increasingly practical proposition [7, 8]. The particular advancement being pursued in this project is the idea of scattershot photon sources, where squeezed states, generated spontaneously from an array of non-linear crystals, are used directly without any feed-forward mechanism [2, 3]. This was initially conceived to make it easier experimentally to show a quantum computation advantage via the Boson Sampling problem [4]. However, the full potential of the scattershot source has yet to be properly explored.

We have made a methodical investigation of the potential for the scattershot source to enhance the performance of quantum interference experiments and quantum metrology experiments. The initial quantum interference results were published in Physical Review A [9] and the quantum metrology results are submitted and are available on the archive [Joshua J. Guanzon, Austin P. Lund, Timothy C. Ralph, arXiv:2105.04135]. In the following sub-sections we summarise these results and discuss extensions we have explored.

3.1 Quantum Interference with a Scatter-shot Source

We begin by describing a passive optical network which takes advantage of perhaps the simplest two-photon variant of the scattershot source to generate quantum interference. In particular, the source is an m mode optical device which non-deterministically generates two separate, but otherwise indistinguishable, photons located anywhere amongst its m channels. Although the photon pair may appear anywhere in the m modes, their location is heralded, and so known. The questions we wish to answer are: (i) can this source be used in a *passive* circuit to reproduce the counting statistics of an arbitrary two mode circuit with single photons entering each input port? Such a circuit is not trivial as it exhibits quantum interference of the Hong, Ou, Mandel (HOM) type [10]; and (ii) if so, is an improvement in sampling rates predicted? We answer both these questions in the affirmative.

We have been able to show, for all possible inputs from the two-photon scattershot source, there exists a passive circuit which can interfere the two photons together as if they were incident on an arbitrary beam-splitter. The protocol works in the following way (see Figure 8). Given the parameters of the beam-splitter, a specific m mode optical circuit is constructed. The scatter-shot source sends photons into the circuit, shot-by-shot, which are counted by single photon detectors at the outputs. The data is analysed in the following way: (i) shot-by-shot, if a pair of photons is heralded in separate modes, then, as a function of the location of the pair, half of the m output detectors are labelled as A, and the other half are labelled as B; (ii) given such an event, the number of photons counted in the A modes is recorded as the number of photons exiting the upper port of the beam-splitter and the number of photons counted in the B modes is recorded as the number of photons exiting the lower port of the beam-splitter; and (iii) if a pair of photons is not heralded in separate modes the attempt is discarded. The specific circuit for $m = 4$ is shown in Fig.9. The beamsplitters in this figure have transmission ratios given by $\eta_1 = \sin^2\theta/[2+\cos(2\theta)]$, $\eta_2 = 2\sin^2\theta/[5+\cos(2\theta)]$, and $\eta_3 = \sin^2\theta/3$.

We now address our second question as to whether this device provides an experimental advantage in terms of sampling rate over more straight forward systems, such as a simple array of beam-splitters. We first analyse what is optimal for the two-photon scattershot source consisting of an array of non-linear squeezing crystals and photon detectors. Each crystal, upon pumping, has a chance of generating a pair of photons through spontaneous parametric down conversion. One of the photons is funnelled to a photon detector, which heralds the existence of the other photon. The heralded photon can then be run through the optical circuit, before also being measured by the detectors. We only accept situations where two photons are heralded at the same time in two separate modes. The total squeezed state for an array of m SPDCs is

$$|\Psi\rangle = \bigotimes_{q=1}^{m} |\psi\rangle_q = \left(1-\chi^2\right)^{\frac{m}{2}} \prod_{q=1}^{m} \sum_{n=0}^{\infty} \chi^n |n\rangle_q |n\rangle_q. \tag{1}$$

Now, the probability of heralding two photons and nothing elsewhere, say in the first two modes $|\Phi\rangle = |11\rangle_1 \bigotimes |11\rangle_2 \bigotimes_{p=3}^{n} |00\rangle_p$, is given by

$$|\langle\Phi|\Psi\rangle|^2 = (1-\chi^2)^m \chi^4. \tag{2}$$

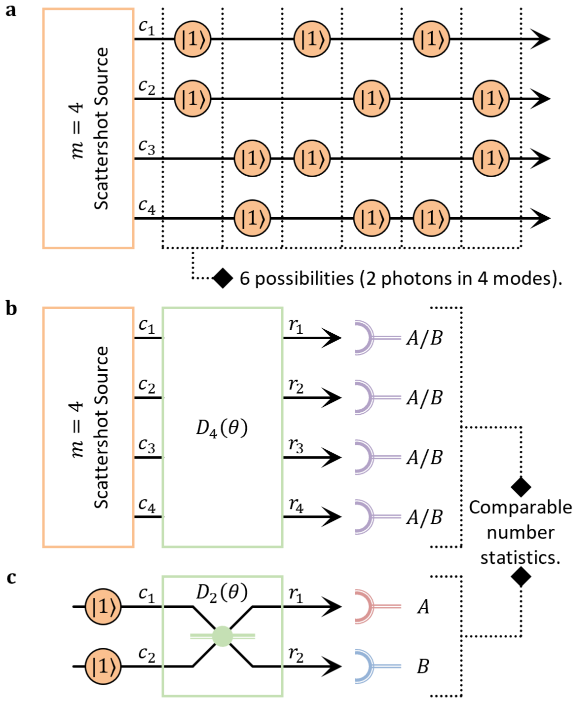

Figure 8: **a** The two-photon scattershot source injects two individual photons randomly into m modes (here $m = 4$), which has $m(m-1)/2$ possible configurations. **b** We show that the counting statistics of the passive linear optical network $D_m(\theta)$ with m photon detectors replicates the beam splitter $D_2(\theta)$'s two-photon interference effect **c** for all possible input configurations, if we judiciously label the output detectors depending on the input.

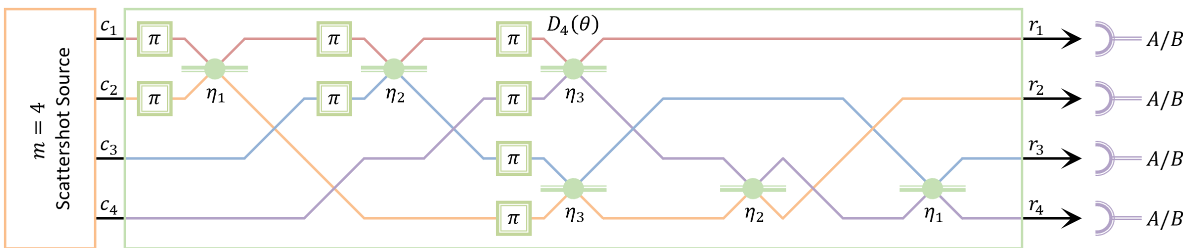

Figure 9: Circuit decomposition of D_4, composed of beam splitters with η_i transmission ratio and π phase shifters.

However, in our D_m, we are allowed to herald two photons anywhere in the m possible modes, for which there are $\binom{m}{2} = m(m-1)/2$ possible allowed inputs. Hence the net probability of success is given by

$$\mathrm{P}_m(D_m) = (1-\chi^2)^m \chi^4 \frac{m(m-1)}{2}. \tag{3}$$

For comparison let us consider an alternative strategy where we simply build $m/2$ versions of our simple beam-splitter in parallel and inject photons from our source into them. We call this circuit L_m. Now the two photons must be heralded in the correct ports such that they meet at one of the beamsplitters. There are hence only $m/2$ possibilities and so the total probability of success is

$$\mathrm{P}_m(L_m) = (1-\chi^2)^m \chi^4 \frac{m}{2}. \tag{4}$$

It is clear that for all possible sizes of the system that D_m provides a better probability of success compared to L_m, and this ratio increases with increasing m. Hence D_m provides a much faster sampling rate compared to L_m.

We can also consider modifying the source itself to work in coincidence. In this situation, we don't funnel one half of the photons into heralding detectors, instead the two output ports of the SPDC crystals are connected directly to the two input ports of a beam-splitter, and again we consider a large, parallel array of such beam-splitters. In this case, we only need a single crystal to generate a $|11\rangle$ pair, which changes the non-linear factor in Eq. (2) from χ^4 to χ^2. Since there will be a total of m squeezing crystals and m beam splitters in the system L'_{2m}, this means the net probability of success is

$$\mathrm{P}_n(L'_{2m}) = (1-\chi^2)^m \chi^2 m. \tag{5}$$

Such a coincidence set-up is less versatile than the heralded systems we have been considering so it is perhaps unsurprising that for smaller m values and system sizes, this L'_{2m} configuration has a higher sampling rate over D_m. However, above $m = 2/\chi^2 + 1$, D_m once again provides a better sampling rate over L'_{2m}, where the ratio of this advantage grows as m increases.

This result shows another example where, at least in principle, a scatter-shot source can show an advantage, albeit in a simple situation. In the next section we seek to extend these results to larger photon numbers.

3.2 Attempts to Generalize Quantum Interference to Higher Photon Numbers

We wish to investigate whether there exists a linear optical network $B_m(\theta)$, with m ports, which allows one to control the amount of quantum interference between photons, irrespective of which ports the photons entered into. We are restricting ourselves to passive linear optical networks, made from experimentally simple beam splitters and phase shift elements. This is because if we could use active optical elements with feedforward mechanisms we could just turn a scattershot source into a fixed photon source, which defeats the purpose of this line of investigation. In the previous section we found a highly symmetric network $M_m(\theta)$ which does this, but only for two photon inputs from the scattershot source [9]. In this section we outline our endeavour to extend this controlled quantum interference result beyond just two photons.

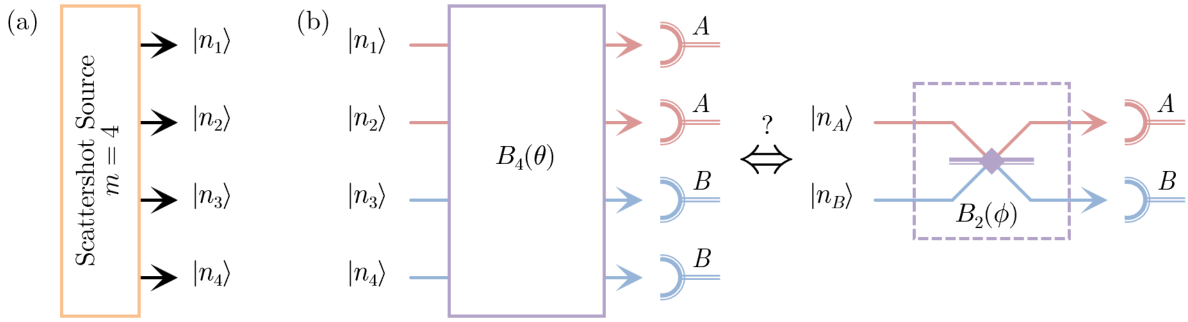

Figure 10: (a) The scattershot source can generate a random distribution of photons, here for $m = 4$ modes. (b) We investigate whether it is possible for an m multimode optical network, here $B_4(\theta)$, to emulate the number statistics of a beam-splitter $B_2(\phi)$, given we group the output and input ports as A/B.

Overview of Our Approaches: We want to find an m multiport linear optical network $B_m(\theta)$ which can take the input from a scattershot source $|n_1 \cdots n_m\rangle$, and replicate the number statistics $\mathbb{P}$ of a standard beam-splitter $B_2(\phi)$ with $|n_A n_B\rangle$. Ideally, we want $\mathbb{P}$ to be the same for all possible inputs, for example for $m = 4$ in Fig. 10 this is all cases where $n_1 + n_2 = n_A$ and $n_3 + n_4 = n_B$ is true. Note ϕ is the transmission coefficient of the beam-splitter, but also determines the amount of quantum interference experienced by the input photons; θ plays this role for B_m. Even though the interference of photons on a beam-splitter seems simple, it is a vital building block towards constructing more complicated optical quantum computing systems.

Our previously discovered symmetric network $M_m(\theta)$ does not sufficiently act like a beam splitter for more than two photons. Fig. 11 is a comparison of the number statistics, we can see that it does manage to replicate two different points labelled I and II; however it doesn't contain other important points such as III where complete suppression of the A^2B^2 measurements occurs.

Numerical Search: We implemented three different search algorithms to explore the space of linear optical networks (described by unitary matrices), as shown schematically in Fig. 12(a-c). They all work to find the best network whose number statistics minimises the amount of error E compared to the number statistics we want. We verified these algorithms by asking it to find a circuit for points I and II for all $|22\rangle$ type inputs, and it can rediscover the M_4 network (since it has $E = 0$). Interestingly, if we then use these algorithms for point III, it will again tell us that M_4 is the best network, however this time E is non-zero.

Another question we explored is whether the task is possible if we start with separable photon inputs, for example $|1111\rangle$. Unfortunately, as shown in Fig. 12(d) and (e) we cannot find any network which can satisfy point II with zero error, even granting the network plenty of extra modes or ports to work with. These algorithms give similar results for the three photon input case as well. Since it appears we can't replicate certain key points using passive linear optics even in the simplest three and four photon cases, this suggests it is unlikely there exists a $B_m(\theta)$ that can replicate all the points with any number of photons.

Analytical Analysis: We expect that if such a $B_m(\theta)$ network exists, then it surely has some kind of inbuilt symmetry as we want it to be input invariant in some sense. It seems likely, on physical and mathematical grounds, that such a network has the identity in it for some θ

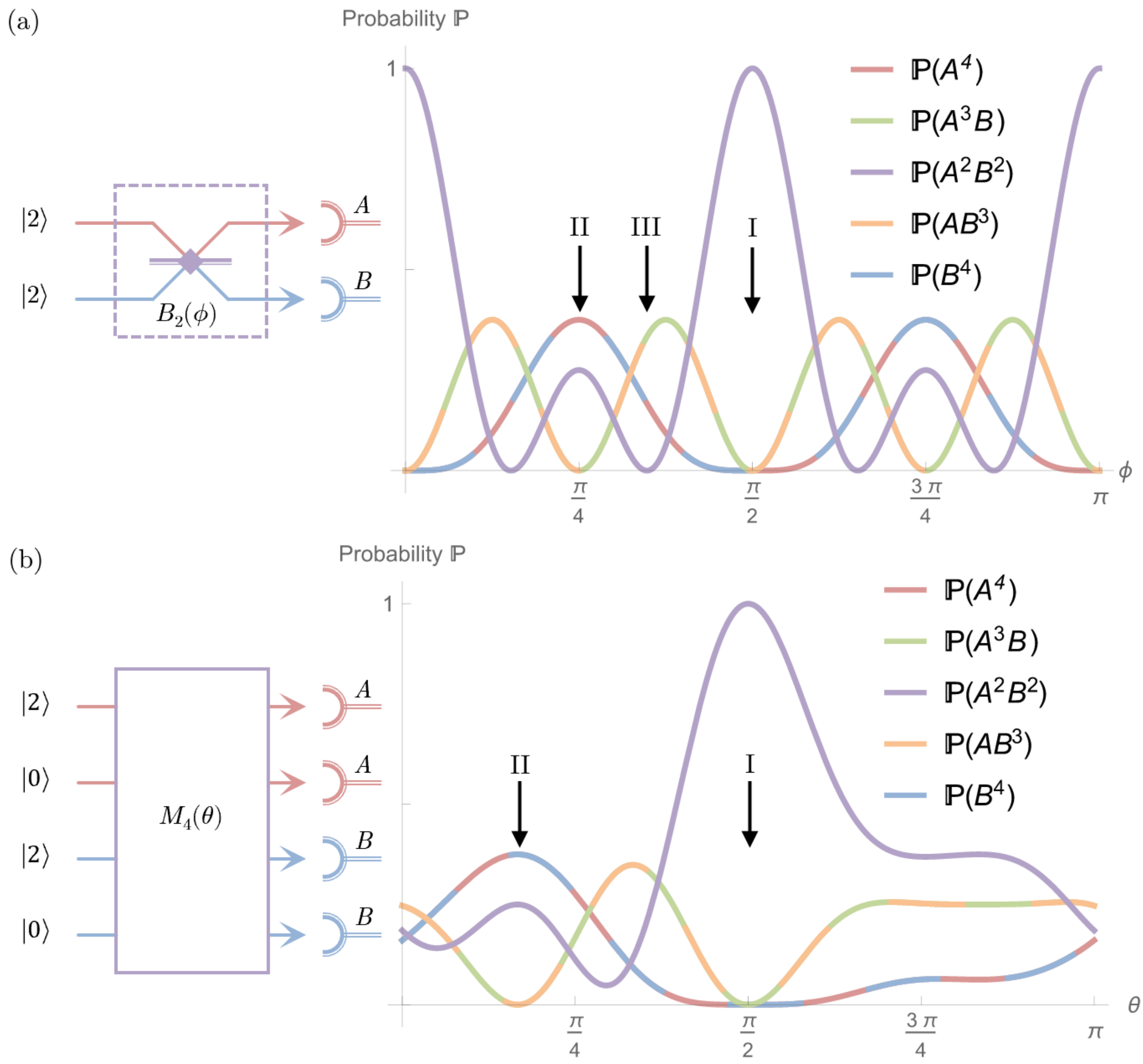

Figure 11: (a) Number statistics of $|22\rangle$ photons into a beam-splitter $B_2(\phi)$. (b) Number statistics of $|2020\rangle$, $|2002\rangle$, $|0220\rangle$ and $|0202\rangle$ photons into our highly symmetric network $M_4(\theta)$, from previous results. Note $\mathbb{P}(A^jB^k)$ refers to the probability that j and k photons were measured at the A and B labelled detectors, respectively. The statistics in (b) are unable to reproduce all the interference features present in (a)

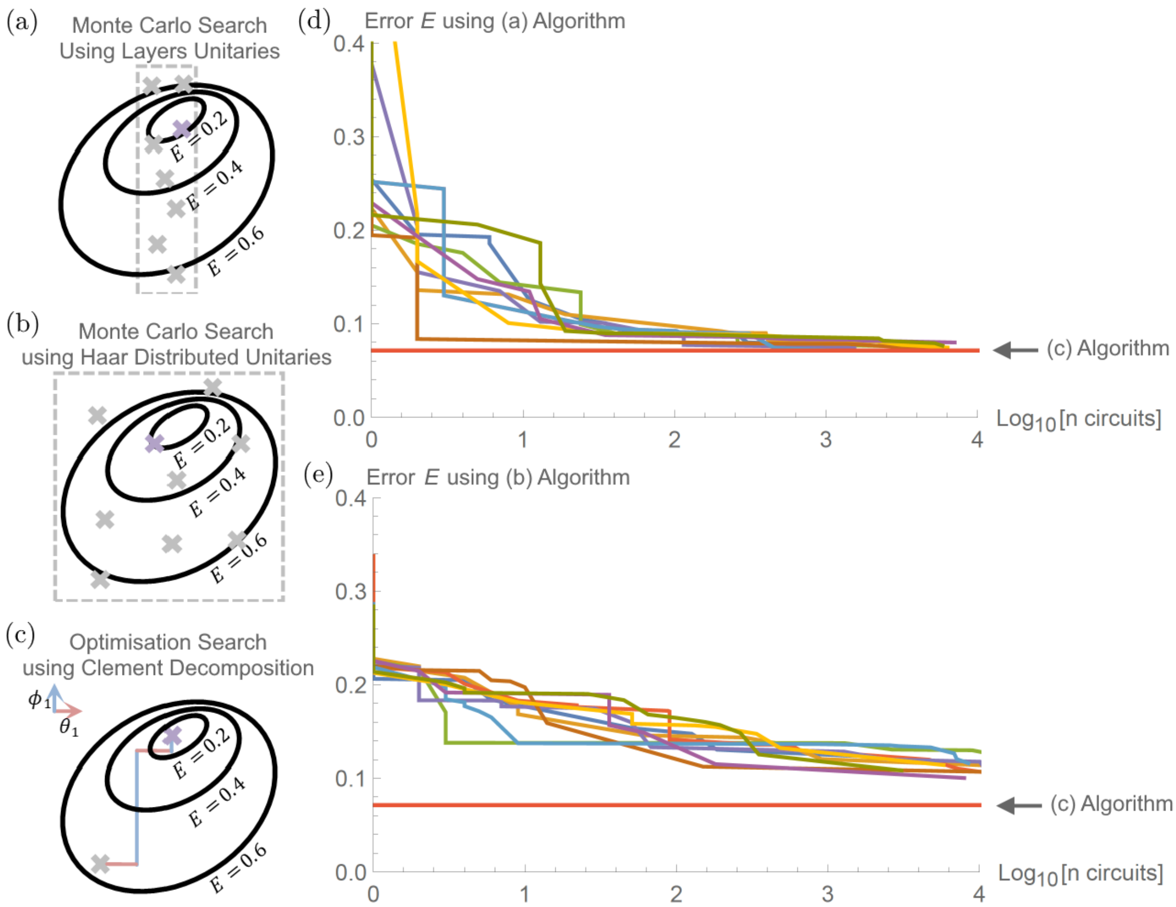

Figure 12: Schematics of the different search algorithms are given in (a), (b) and (c). An example of the Markov chains (or threads) of how (a) and (b) converge to minimise the number statistics error E is given in (d) and (e), respectively; the red horizontal line is the best circuit found using the optimisation (c) method. Note this example is finding a circuit for point II using $|1111\rangle$ type input.

value (i.e. a setting where it lets photons simply pass through it unchanged). If it does have the identity, then we can actually prove analytically, at least for the $m = 4$ mode case, that such a network must be our previous symmetric network $B_4(\theta) = M_4(\theta)$; which we know doesn't work without some error.

All these results suggest that it is not possible to find a passive multimode network which always acts like a beam-splitter irrespective of where the photons enter. Furthermore, the symmetric network $M_m(\theta)$ we found previously is perhaps the best we can do from an error minimisation perspective. These results should not necessarily be taken as an absolute no-go for solving this problem as our search is still quite constrained in terms of the physical arrangement of, and particular assumptions about, the squeezers, heralding and passive optics. Future work could examine different configurations.

3.3 Quantum Metrology with a Scatter-shot Source

Metrology, is the study of measurement accuracy and precision in a broad range of experimental contexts. Quantum metrology considers these factors in situations where the ultimate limits are given by quantum mechanics. Measurement probes that exhibit non-classical properties, such as quantum entanglement or squeezing, can have advantages in measurement precision [11].

Given this, it is interesting to consider whether boson sampling-like systems are useful for metrology. In this regard, there have been recent papers studying a multimode metrology scheme based on Quantum Fourier Transformation (QFT) interferometers, which shows a quantum advantage up to certain network sizes [12]. Like boson sampling, these devices use single photon inputs and the QFT induces number-path entanglement to beat the classical precision limit. This scheme with QFT interferometers has been implemented experimentally in various small sizes [13].

Our research aims to translate the ideas from scatter-shot boson sampling for scattershot multimode metrology purposes. We focus on scattershot sources as the main stage of a single-parameter estimation scheme and analyse and contrast different multimode interferometers, including QFTs.

We begin with the structure of the metrology problem and interferometers we have investigated. In a metrology experiment, we want to maximise our knowledge of a fixed unknown phase shift ϕ, while minimising the amount of resources it takes to get that information. First, consider the standard two-mode Mach–Zehnder interferometer (MZI) given by the unitary

$$Y_2(\phi) \equiv X_2 Z_2(\phi) X_2^\dagger = \begin{bmatrix} \cos(\phi/2) & \sin(\phi/2) \\ -\sin(\phi/2) & \cos(\phi/2) \end{bmatrix}, \tag{6}$$

where the unknown phase shift $Z_2(\phi)$ is applied to only one of the modes, and is conjugated by fixed 50:50 symmetric beam-splitters X_2. This is shown visually in Fig. 13(a), where we have included a controllable known phase shift θ as a reminder that the overall phase shift could always be tuned close to an experimentally convenient value (e.g. $\phi + \theta \approx 0$ such that the overall scattering is close to the identity $Y_2(0) = \mathbb{I}_2$). However, for mathematical convenience, we will set $\theta = 0$ and just remember we can always tune the phase shift.

Now, consider the m-mode extension of this interferometer

$$Y_m(\phi) \equiv X_m Z_m(\phi) X_m^\dagger, \tag{7}$$

where the phase shift $Z_m(\phi)$ is over half of the modes, and X_m is a fixed linear optical network, analogous to the 50:50 beam-splitters in the two-mode MZI, but X_m could potentially mix between all modes. This arrangement is shown in Fig. 13(b). Using this network construction we will explore different X_m networks which will allows us to extend particular properties of the standard MZI to multiple modes. It is important to note that the treatment of the phase shift $Z_m(\phi)$ as a resource is different to the previously mentioned Ref. [13], where they consider the best way to divide up a fixed total amount of phase amongst many modes (i.e. the phase shift can be different on each mode depending on the strategy employed). In our case, the phase shift applied on the modes is the same; physically, we are just considering a straightforward scenario where the sample being measured, such as a piece of glass or ampule of gas, is uniform and simply overlaid upon half of the modes.

One benefit of investigating interferometers of this type is that a separable stack of $m/2$ MZIs

$$Y_m^{(\mathrm{sep})}(\phi) \equiv \oplus_{j=1}^{m/2} Y_2(\phi), \tag{8}$$

is an interferometer that fits the phase structure as shown in Fig. 13(c), where effectively $X_m^{(\mathrm{sep})} = \oplus_{j=1}^{m/2} X_2$ with some trivial rearrangement of the modes. It is known that photon inputs into a MZI can show quantum enhanced detection, as long as the photons are not all in one port [14]; hence scaling this system by $m/2$ copies effectively expedites determining ϕ. Alternatively, $Y_m^{(\mathrm{sep})}(\phi)$ can be thought of as being separated temporally, in other words just using one standard MZI with $m/2$ samples. Given independent samples, the total information will be just the sum of the individual measurements. It is this intuitive interpretation which we use to fairly compare different sized multimode interferometers with the same structure, as we can use separable interferometers with equivalent number of phase shifts as a standard metric.

The Cramér-Rao bound constrains the achievable precision of an unknown variable ϕ as follows

$$(\Delta\phi)^2 \geq \frac{1}{\mathcal{F}}, \tag{9}$$

where $\mathcal{F}$ is the Quantum Fisher Information (QFI) [15]. Classical interferometers can not beat the shot-noise limit (SNL) of $(\Delta\phi)^2 \geq 1/n$, where n here is the total number of probes or photons in our case. In contrast, it is known that quantum interferometers can approach the higher precision Heisenberg limit of $(\Delta\phi)^2 \geq 1/n^2$, through quantum entangled photons or squeezed states.

Suppose we know that an interferometer is described by the unitary operator $\hat{U}(\phi)$, where an input state ρ is acted upon as follows

$$\rho(\phi) = \hat{U}(\phi)\rho\hat{U}^\dagger(\phi), \quad \hat{U}(\phi) = e^{-i\hat{H}\phi}, \tag{10}$$

in which $\hat{H}$ is the generating Hermitian operator for $\hat{U}$. We can then use the following equation to calculate the QFI

$$\mathcal{F} = 4(\Delta\hat{H})^2 = 4(\langle\vec{n}|\hat{H}^2|\vec{n}\rangle - \langle\vec{n}|\hat{H}|\vec{n}\rangle^2), \tag{11}$$

since our input from the scattershot source is a pure state [16], as a tensor product of Fock states

$$|\vec{n}\rangle \equiv |n_1\rangle \otimes \cdots \otimes |n_m\rangle \equiv |n_1 \cdots n_m\rangle. \tag{12}$$

This computation is convenient as it allows us to determine the QFI just from the input state.

For our metrology considerations, the two input ports of an MZI are permutationally invariant, in the sense that the inputs $|n_1 n_2\rangle$ and $|n_2 n_1\rangle$ will provide the same amount of extractable information about ϕ; this is the natural consequence of the 50:50 beam splitters X_2. In our multimode case, let us suppose the scattershot source gave a particular input of $|\vec{n}\rangle \equiv |n_1 \cdots n_m\rangle$, input invariance would mean the QFI remains the same if we switch any two modes $n_j \leftrightarrow n_k, \forall j, k$. Since the scattershot source generates photons at random inputs with equal chance in all modes, it would be advantageous if we can find a $Y_m(\phi)$ interferometer which has this input invariance property for all modes. Clearly for $Y_m^{(\mathrm{sep})}(\phi)$ the first mode interacts with the second mode, but doesn't interact with the third mode, hence it does not have input invariance. One may speculate that this property exists for

$$Y_m^{(\mathrm{uni})}(\phi) \equiv F_m Z_m(\phi) F_m^\dagger, \tag{13}$$

where we replace $X_m^{(\mathrm{uni})} = F_m$ in Fig. 13(b) with a uniform scattering device such as the QFT or Hadamard (Sylvester) transformation. These are optical devices in which the associated scattering matrix has elements of the same uniform magnitude, which means if a single photon is injected into any of the input ports, there is an equal chance of measuring it in any of the output ports. However, we find that uniform interferometers do not result in the symmetry which we are looking for; hence finding an interferometer with input invariance is not an immediately obvious problem to solve.

We propose using a symmetrising transformation T_m, which is used to create the interferometer

$$Y_m^{(\mathrm{sym})}(\phi) \equiv T_m[\oplus_i^{m/2} Y_2(\phi)] T_m^T, \tag{14}$$

that has a symmetrical scattering matrix with very similar properties as $Y_2(\phi)$. This construction is shown in Fig. 13(d), where the symmetric interferometer clearly has the same overall phase structure as the other interferometers, however with $X_m^{(\mathrm{sym})} = T_m(\oplus_{j=1}^{m/2} X_2)$ and some trivial rearrangement of the modes. We show that this is an optimal way of mixing the modes such that it is input invariant. In other words, we can show that the symmetric interferometer will *always* give a quantum enhanced detection using scattershot sources. As a consequence of this, we show that $Y_m^{(\mathrm{sym})}(\phi)$ is more likely to give more information than $Y_m^{(\mathrm{sep})}(\phi)$ for finite sample sizes. Finally, we note that the symmetric interferometer can actually be implemented with temporal modes and one MZI, where T_m describes how the different temporal modes should interact together; hence the experimental implementation of this scheme to large mode numbers is feasible with the system being developed in the experimental part of this project.

As we have argued previously the separable interferometer is the natural baseline to compare with other multimode interferometers of similar size and structure. The QFI in this case is

$$\mathcal{F}^{(\mathrm{sep})} = n + 2 \sum_{j=1}^{m/2} n_{2j-1} n_{2j}, \tag{15}$$

The uniform interferometer uses QFTs in a manner like that of previous papers, but actually doesn't lead to the required symmetry that maximises the benefits of using scattershot sources.

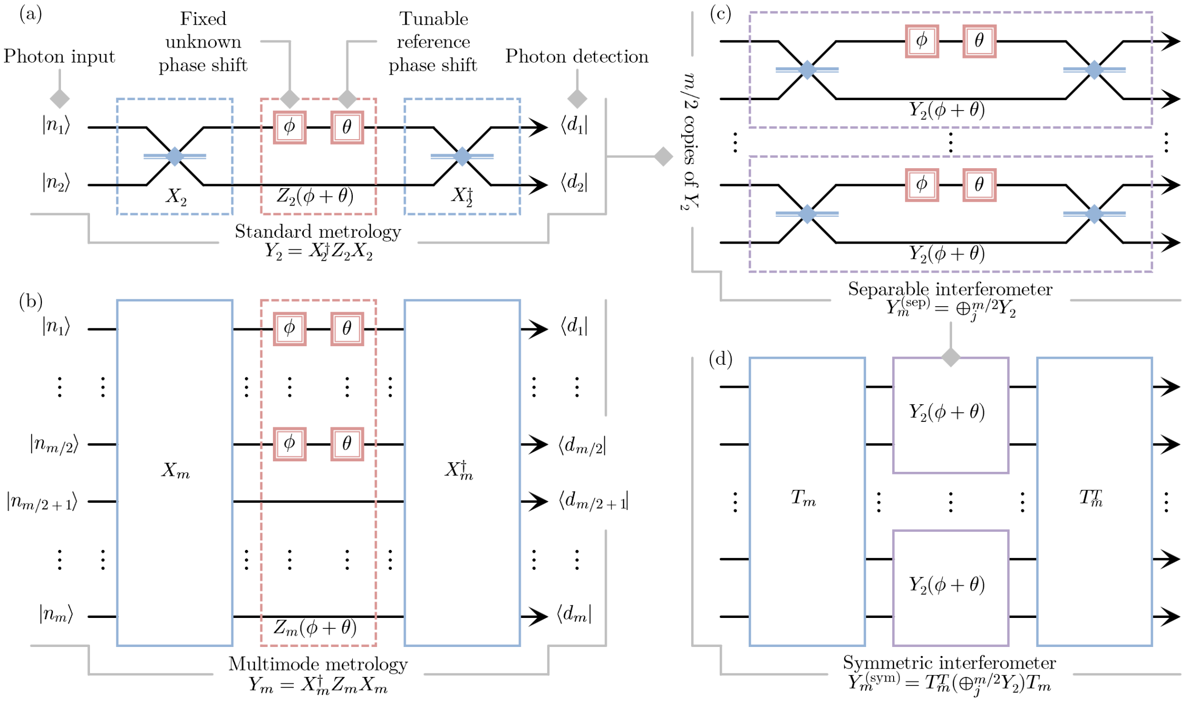

Figure 13: (a) A standard metrology experiment to determine ϕ, using a Mach–Zehnder interferometer, photon inputs and photon counting detectors. (b) We explore the natural multimode version of this standard setup, where we investigate interferometers with phase shifts applied to half of the m modes. (c) One multimode interferometer of this type is made from stacking together $m/2$ copies of Mach-Zehnder interferometers. However, the amount of information gathered about ϕ depends on which ports the photons are injected into. (d) We will show that we can create a symmetrising transformation T_m, which results in all mode being treated equally, just like in the standard two-mode metrology experiment.

Table 2: Summary of the Quantum Fisher Information associated with the three multimode interferometers under investigation for the example of two single photons into four modes $m = 4$. This demonstrates the input invariance of the symmetric interferometer and that on average all three will give the same amount of information, a result that generalizes to higher mode and photon numbers.

Input	$\|1100\rangle$	$\|1010\rangle$	$\|1001\rangle$	$\|0110\rangle$	$\|0101\rangle$	$\|0011\rangle$	Avg.
Separable	4	2	2	2	2	4	8/3
Uniform	3	2	3	3	2	3	8/3
Symmetric	8/3	8/3	8/3	8/3	8/3	8/3	8/3

The QFI in this case is

$$\mathcal{F}^{(\text{uni})} = n + \frac{8}{m^2} \sum_{j=1}^{m/2} \sum_{k=1}^{m/2} \frac{n_{2j-1} n_{2k}}{\sin^2\left(\frac{\pi(2k-2j+1)}{m}\right)}. \tag{16}$$

With the symmetric interferometer we can prove that the overall network symmetry means that all possible photon input configurations lead to a quantum enhancement from scattershot sources. The QFI in this case is

$$F^{(\text{sym})} = n + \frac{1}{m-1} \sum_{j=1}^{m} \sum_{k \neq j}^{m} n_j n_k. \tag{17}$$

The QFI of the three interferometers shows that all three can beat the classical shot-noise precision limit and in the asymptotic limit of large numbers of samples all three will give the same amount of information – that is on average they have the same QFI. However, shot by shot the symmetric interferometer always gives a better than shot-noise result, whilst this is not true for the other interferometers. These results are illustrated for a particular example in Table 2.

Finally we implement Monte Carlo simulations to contrast the separable and symmetric interferometers in regimes of finite sample size that may be of experimental interest. In particular we show that there are situations where, if the sample size is limited, it can be an advantage to use the symmetric interferometer. On the other hand for other sample sizes the separable inteferometer has an advantage. As would be expected from their equal averages, the two types of interferometer perform equally in the asymptotic limit.

4 Advances in Scatter-Shot Source

4.1 Summary of the advances

As part of this project, several key performance enhancements have been done on the source of scatter-shot states. We have

- designed and manufactored a custom poled nonlinear crystal for generation of pure and frequency uncorrelated photons that requires no spectral filtering; The corresponding test setup is in the process of an upgrade to match the new parameter range, with crystal testing scheduled for immediate future;
- developed the readout electronics of SNSPDs with custom-designed cryogenic amplifiers and confirmed the capability of successful operation of at least four devices, providing significantly improved timing characteristics of the system without noticeable detrimental impact on the system capacity to hold the necessary cryogenic temperatures;
- developed and set-up a free-space optical circuit for photon switching and tested it via Hong-Ou-Mandel interference, confirming the excellent capability of the circuit to route and delay single photons without affecting their purity and quality of the state.

We describe these results in more detail below.

4.2 Apodisation of periodic poling

Our photon source is based on SPDC from a pp-KTP nonlinear crystal. The key properties of the source—the length of the crystal, the poling period, the focusing of the pump laser beam, the lens configuration that determines the photon mode collected, the spectrum of the pump—determine the phase matching conditions and ultimately the spectral distribution of the pair of downconverted photons [5]. We have engineered these properties such that the photons' joint spectrum—known as the joint spectral intensity (JSI)—is *separable*, i.e. not entangled, to a first approximation—see Fig. 14. Spectrally unentangled photons will be necessary for the high-quality nonclassical interference that forms a central part of the BosonSampling protocol.

The central lobe in the JSI (Fig. 14, right) shows that most of the photon intensity corresponds to a degenerate, separable spectral signature. The remaining issue is that the typically-used periodic poling (Fig. 15, top) is a square wave in space, which leads (via the Fourier transform) to an anticorrelated sinc function in the joint spectrum of the photons. This small amount of correlation produces some mixture in the states of the individual photons, and thus decreases the interference visibility observable when interfering photons are generated in different downconversion events. It is possible to use spectral filters to remove all but the central lobe, but this reduces the heralding efficiency (i.e. increases loss) which is undesirable for photonic quantum protocols.

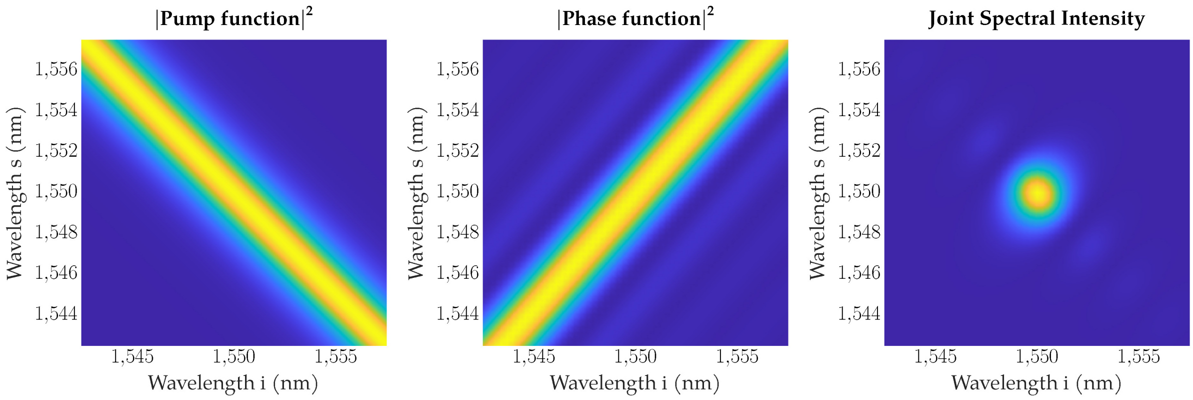

Figure 14: Simulation of the Joint Spectral Intensity produced by downconversion in a crystal with the typically-used square-wave periodic poling. The domain width of the crystal is 23.10 μm and the crystal length is 15.0 mm. The pump has a bandwidth of 0.79 nm centered at 775 nm. These values are experimentally relevant. The purity of each photon's quantum state is predicted to be 79.57%. As this is significantly less than 100%, a compromised interference visibility would be expected when using these photons.

Fortunately, there is a method that can eliminate this remaining correlation. Called *JSI engineering*, it is the custom shaping of the poling function (Fig. 15, bottom) to produce a favorable biphoton joint spectrum. This process is known as *apodisation*. The overall concept has been proposed previously, but achieving high performance remains an art that the community has not yet mastered. This is because the physical limitations on the poling process (i.e. engineering limitations in implementing the poling process) place extra constraints on the determination of the optimal poling function. Furthermore, this process has multiple goals/constraints—while optimising for the desired spectrum, one must also maintain as much brightness as possible, maintain the central wavelengths of the SPDC photons, and control their spectral widths and spatial modes at desirable conditions. For this reason, the design and implementation of the numerical optimisation procedure to calculate the desired poling period is not trivial. In this context, we look to obtain the best possible results in designing the poling of our next generation of sources.

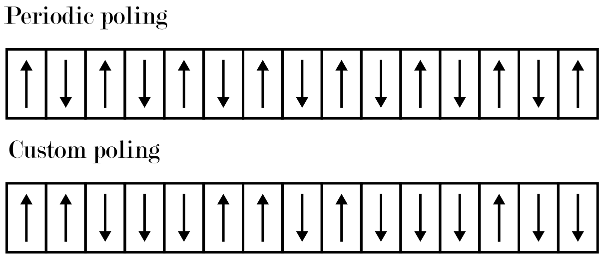

Figure 15: Representation of periodic and custom poling. The long rectangles denote the SPDC crystal, through which the pump beam passes from left to right, say. In periodic poling (top), each of the nonlinear domains alternates in orientation. This square-wave pattern leads to a phase matching function (Fig. 14) with a sinc profile. By allowing custom (in general, non-periodic) orientation of the domains (bottom), then it is possible to engineer a phase matching function with a Gaussian profile.

To do this, we employ a technique modified from Dosseva *et al.* [17], in which they used simulated annealing to attempt to find the optimal poling configuration that produced a phase-matching function (PMF) with a Gaussian profile, in a simple configuration. In that work, the purity calculated from the simulated joint spectral intensity (JSI) was reported to be 99.99%. However, these existing results do not apply to our situation, because we need to more faithfully model the focusing conditions, and we want our downconverted photons to be degenerate. After modifying the simulation parameters for degenerate downconverted photons and using a different model [18] to more faithfully simulate the focusing of the pump and downconverted photons, we obtained a predicted purity of 96.81% with our modification of the simulation method. Although this number is slightly lower than that of Dosseva *et al.*, it corresponds to a more realistic and experimentally useful situation and takes into account the constraints listed above.

In the implementation of the modified numerical optimisation method, the cost function was defined as the difference between the PMF obtained from an arbitrary poling configuration and a Gaussian PMF, which is nominally ideal. However, this target requires certain assumptions. We realised the cost function can be modified to instead maximise the purity—the real goal—which involves simulating the JSI and extracting the purity information at each evaluation of the cost function. Although this makes things more complex, with our modified method we were able to obtain a predicted purity of 98.73%, an improvement over our previous result of 96.81%.

The best purity we have achieved is better than the simulated purity achieved in a recent high-end result from another group [19], employing broadly similar techniques and constraints, and so we expect to outperform the interference visibility that they achieved.

The next step was to obtain the custom SPDC crystal from Raicol, the leading manufacturer of poled KTP, according to our poling mask design, and to characterize the new crystal using an in-house built time-of-flight photon pair spectrometer. These steps have been delayed with the ongoing COVID-19 situation, first in the delivery of the nonlinear crystal, then in the repair

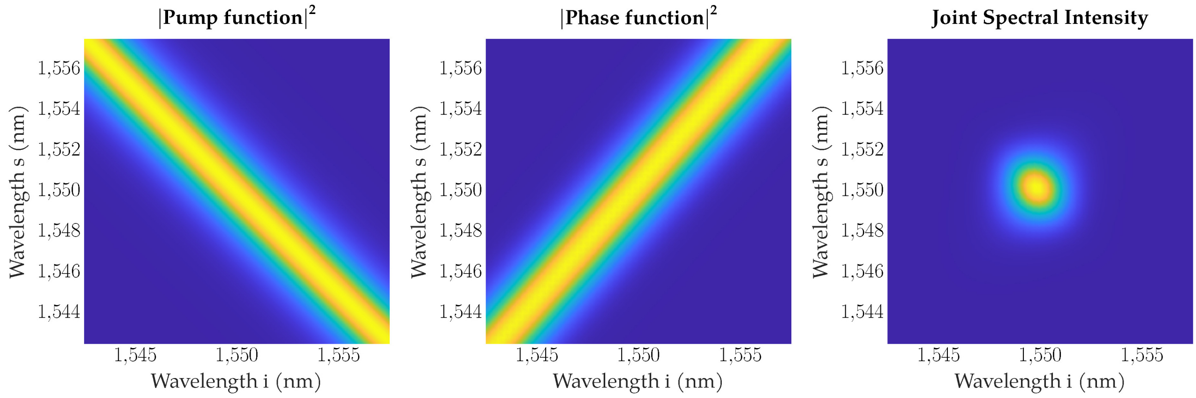

Figure 16: JSI simulation of apodised crystal, from our best numerical optimisation design. The domain width of the crystal is 23.11 μm and the crystal length is 23.6 mm. The pump has a bandwidth of 0.79 nm centered at 775 nm. The purity is predicted to be 98.73%.

and upgrade of the high-power Ti:sapphire picosecond laser required for characterization. While this upgrade is still in progress, the final step would involve characterisation via the two-photon nonclassical interference. We expect to achieve significantly superior performance to our current sources, which are already quite high performance.

4.3 Implementation of readout electronics

The basis of our temporal gaussian BosonSampling protocol, and related applications discussed above, is the ability to interfere photons at time step N with those at time steps $N+1, N+2, \ldots$ (Fig. 2b). The clock cycle is ideally defined by the repetition rate of the mode-locked laser pump, which is ≈ 12.3 ns in our case. However, the limiting factor at the moment is actually the dead-time of the superconducting nanowire single photon detectors (SNSPDs) [7], which is typically $40-100$ ns. This recovery time is primarily determined by the RLC time constant of the detector and readout electronics. In principle, this can be modified by choosing a different resistor configuration, but this reduces the output voltage and thus the signal-to-noise ratio at the inputs of the (room-temperature) amplifiers.

A promising solution is to use cryogenic HEMT (high-electron-mobility transistor) amplifiers to read out the detector voltage outputs (Fig. 17(a)). This allows for reduced detector dead-time and, simultaneously, a high signal-to-noise ratio. Implementing these amplifiers requires careful design not only of the electronics but also the physical and thermal configuration. These latter considerations are to ensure that the amplifier circuitry—for multiple detector channels, with one amplifier per channel—can physically fit in the cryostat and does not provide an excessive heat load at the 0.85 K stage where the SNSPDs sit.

To achieve these goals, we have designed custom cryogenic HEMT amplifiers. Tests of our first-generation devices—implementing a design modified from the group of collaborator Prof. Sven Rogge (UNSW)—achieved pulse widths of under 20 ns—see Fig. 17(b), much lower than what can be achieved with standard room-temperature amplification. However, the operation suffered from several drawbacks: the detection pulse had significant overshooting; the output had to be heavily filtered from additional noise; and no more than two amplifiers could run simultaneously without overheating the 0.85 K stage of the cryostat.

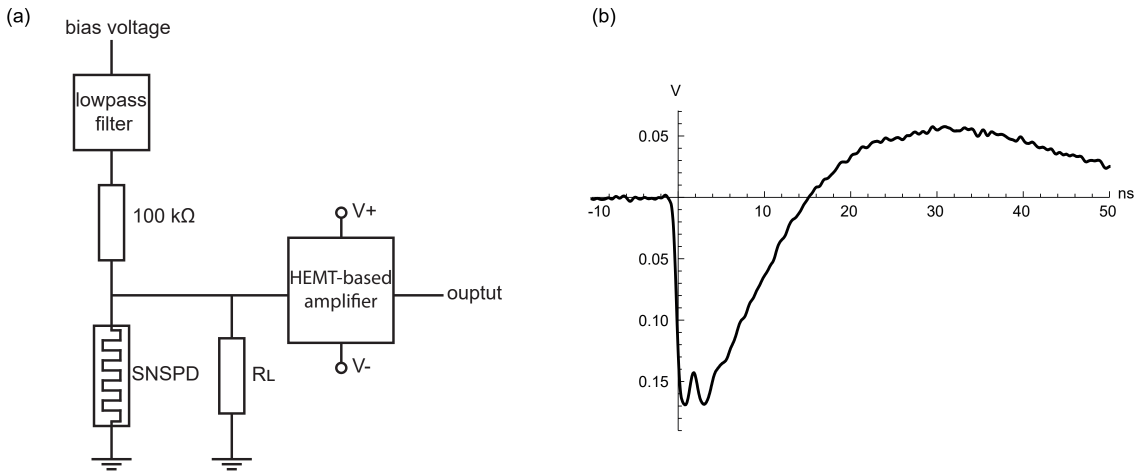

Figure 17: (a) A conceptual diagram of the cryogenic amplification circuit. (b) Output signal trace (voltage vs time) from the first-generation cryogenic amplifier circuit.

Subsequently, we have implemented an improved electronic and physical design. Custom-designed mounting of the corresponding PCBs now allows for the implementation of more robust wiring, which has significantly reduced noise, while also reducing heat transfer to the coldest stage of the cryostat. This change allowed the placement of the amplifiers on the 40K stage of the cryostat without introducing impedance matching problems. The 40K stage has a significantly higher cooling capacity and is expected to allow tens of amplifiers to run simultaneously. In order to find the optimal values of the shunt resistance R_L (that defines the recovery time of the detector), we have implemented several circuits, with R_L varying from 100Ω to 250Ω, to be tested inside the cryostat. The tests confirmed the capability of easily holding at least four cryogenic amplifiers inside the cryostat with only mild ≤ 0.05 K increase in the temperature of the coldest stage, indicating the potential to hold many more devices on board. The new devices showed improved time performance, although further work will require optimization in the electronic wiring and the amplification circuit to remove low-frequency noise and parasitic reflections of the electric pulse between the amplifier and SNSPD.

4.4 Implementation of photon switching

Finally, the applications of our source require the ability to efficiently shift photons from one time bin to another. Development of this capability has been progressing in parallel to other experimental tasks during the entire duration of the project. This upgrade involved the design and implementation of an optical delay line, capable of actively switching photons from different time bins while keeping their properties, such as purity, spectral profile, and indistinguishability intact. This work consisted of the following steps.

1) Choice of the optimal delay method. While the most straightforward way to delay photons is to use optical fibre, this method cannot satisfy our requirements. Fibre introduces a larger amount of loss, significant spectral dispersion, and thermally-induced fluctuations compared to free-space propagation. Moreover, fibre circulators or similar devices required for routing and switching of photons inside and outside the fibre loop introduce a significant

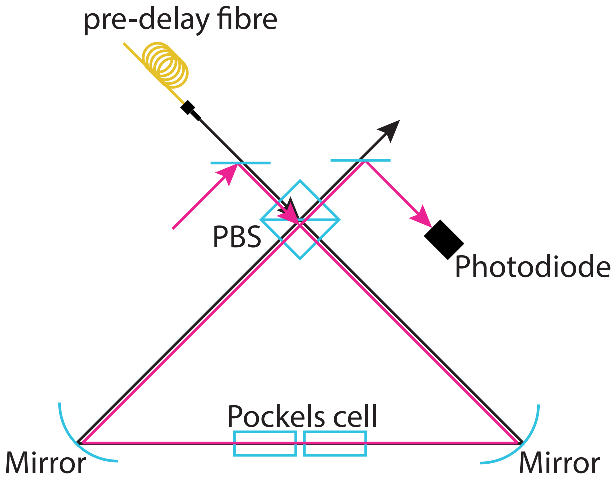

Figure 18: A conceptual diagram of an active optical delay line circuit. Horizontally polarized input photons are transmitted through the PBS and enter the delay loop. Active polarization control realized via a Pockels cell can switch the polarization of photons from horizontal to vertical, if the photon is intended to be delayed by more than one time bin. Switching the polarization state to horizontal again would send the photon out of the loop, thus re-routing it into a different time bin. A fixed-length delay of ≈ 100 ns, realized by optical fibre is used to provide enough time for the electronics to react to the heralding signal and generate the switching signal for the Pockels cell. An interference signal from a separate beam of a different wavelength is used to provide a feedback signal for the active stabilization of the loop length.

amount of loss. Because of these reasons we chose a free-space optical loop architecture as the optical delay line implementation method.

2) Optical loop design. Designing a low-loss optical loop required careful calculation of the spatial mode of the beam propagating inside the loop, according to standard optical resonator stability theory. While traditional optical cavities operate by rejecting the optical modes not compatible with the cavity, the optical delay loop is required to keep all input light as much as possible, for as many round trips as possible. For this reason, the input and output modes, modes inside the loop, and optical component parameters need to be optimized in order to minimize the amount of possible loss due to free-space diffraction. The optical loop consists of a polarizing beam splitter (PBS), acting as input/output port, flat and/or curved high-reflectivity mirrors for beam confinement, and low-loss passive and active polarization switching components. Due to the need of curved mirrors (or additional lenses, although this would introduce further loss due to reflections), the natural spatial eigenmode of the loop exhibits some astigmatism. In choosing the optimal parameters of our loop we managed to reduce the astigmatism of the beam in the area where active polarization switching components are located, at the cost of increased astigmatism at the input to the loop. Increased astigmatism at the input requires a single set of optical components to compensate for it once, while improved astigmatism inside the loop ensures high-quality operation of the switching stage. After careful investigation of the achievable experimental parameters, we chose a triangular layout for our delay loop. The final design consisted of a right-angle isosceles triangle, as shown in Fig. 18, of ≈ 3.6922 m length to match the temporal distance between the scattershot source time bins. The right-angle vertex contained an input/output PBS, while the other two vertices contained two curved high-reflectivity dielectric mirrors with a focal length of $F = 2$ m. Such a configuration provided a stable optical mode propagation with negligibly small astigmatism of $\approx 2.8\%$ and a beamwaist size of ≈ 1 mm at the location of the Pockels cell (see Figure 18).

3) Active stabilisation. Due to the unusually large length of the loop and the requirements of a very precise definition of the time bin, the optical path length of the loop required active stabilization. For this purpose, one of the mirrors was mounted on a piezo-actuated mount and an additional near-IR laser beam was sent inside the loop. The interference signal between the beam that passes through the loop and the one directly reflected from the input PBS was used as the feedback signal for PID control circuit that drove the piezo actuator.

4) Fast switching. While fast in-fibre switching can be easily achieved with an integrated electrooptic modulator (although at a cost of an inevitable loss), high-contrast free-space switching at nanosecond scale is a challenging problem, because it requires fast switching of high (of the order of kilo-volts) voltages supplied to the electro-optic crystal. In our case, we implemented such polarization switching inside the optical loop using a Pockels cell based on two Rubidium Titanyl Phosphate RTP crystals (from Leysop). We used high-voltage Pockels cell drives developed by BME Bergmann, which promise one of the highest rise and fall times, of the order of 5 ns when used in conjunction with RTP material. In our tests, we managed to achieve a minimum switching pulse duration of 20 ns using the Pockels cell system already available in the lab. Such duration of the switching pulse is larger than the separation time between the two modes of the source. This limitation would affect the photon distribution across the modes for the cases when two neighbouring modes are populated, but only one of

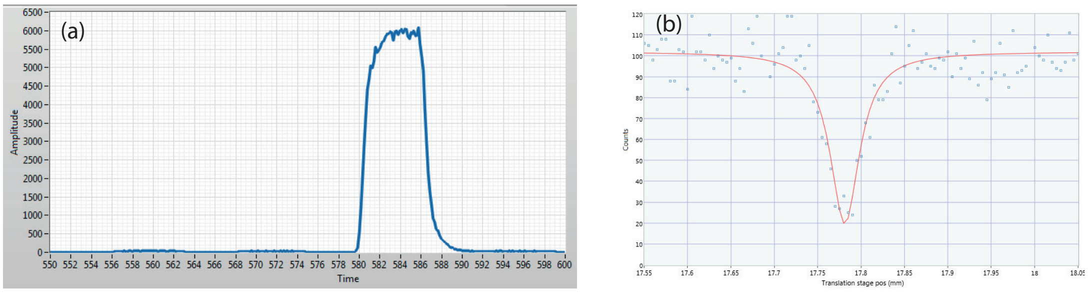

Figure 19: Characterization of the active switching delay loop. (a) A measurement of photon switching. Photon arrival time to the detector is delayed by two time bins, ≈ 24.6 ns, from ≈ 559 ns to ≈ 584 ns, with very low probability of detecting photon in the original or neighbour time bin. Signal to noise contrast is approximately $200 : 1$ in this example. (b) Hong-Ou-Mandel interference between photons separated by two time bins, realized by delaying the earlier photon with the active delay loop. Experimentally observed interference visibility is 0.81 with uncertainty estimated to be around 0.3. Maximum theoretical visibility is $0.82 - 0.84$ depending on the model used.

them needs to be switched. A way to overcome this limitation is to use a smaller-sized electrooptic crystal, which will require lower switching voltages and thus faster operation. Due to the careful design of the optical loop, we estimate that we can easily transit from the standard RTP crystal with a transverse cross-section of 4×4 mm to a one that has a cross-section of 3×3 mm, without introducing any additional loss due to beam clipping. This step, together with an upgrade of the BME Bergmann Pockels cell driver, permitting even faster operation, was significantly delayed due to the ongoing COVID pandemic. While we have recently obtained the new devices, their installation and test fell out of the timeline of this project. Nevertheless, we could use the existing tools to perform preliminary testing and verification of the active delay line.

Characterization of the overall assembled setup showed the following results. We have achieved 93% loop transmission, with potential sources of loss already identified. Most noteworthy, we observed over $200 : 1$ contrast in the switching of photons from one time bin to another. This number is comparable with the maximum performance of an RTP material and achieving it sets a great starting point for high-quality time mode manipulation. Finally, we tested the visibility of the non-classical interference between photons separated by two time bins. We observed interference visibilities of over 0.8, which is very close to the ideal interference visibility of $0.82 - 0.84$, obtainable with the specific pp-KTP crystal used in the test. This result highlights the excellent property of the optical loop in keeping the photon indistinguishability and purity high and is crucial for future applications of the scatter-shot source. Given these results, we expect to observe close to unit interference visibility without any spectral filtering once the new design crystals have been characterized and incorporated into the source setup.

4.5 COVID-19 situation

COVID-19 pandemic continues to impact significantly research and academic activities in Australia. At present, under Australian federal government, Queensland state government, and

Griffith University regulations, our experimental research laboratory remains open, albeit with some operating restrictions. Therefore, we continue experimental research. However, we are experiencing slower-than-usual operation because of delays in shipping new, repaired, maintenance, and consumable items. This includes maintenance and repair of equipment critical to this project, such as cryogenic refrigerators (damaged due to a power surge in 2020) and high power laser maintenance and upgrade, and equipment (custom pp-KTP crystals, amplifiers, Pockel cell and driver) delivery. Furthermore, the University has put in place operating restrictions concerning personnel (lab personnel, and university support staff) that is also slowing progress a little, and regular short-term state-wide lockdowns introduce significant short-term interruptions of laboratory activity.

The situation at the University of Queensland is similar. The University is not closed but all staff are intermittently being advised or required to work from home. As a result, many meetings regarding collaboration and progress in the theoretical aims have been carried out via video conferencing. However, this did not lead to significant delays.

5 Summary and Future Directions

In this report, we have presented the results of the development of a scatter-shot source of heralded photons and its new applications. Our scattershot source demonstrated a remarkable capability of generating many photon states distributed across many temporal modes. Demonstrated examples include ≈ 115 correlated photon pairs generated within 39^3 temporal modes. For the applications that require lower number of temporal modes, we demonstrated, for example, scatter-shot states of 12 to 18 photon pairs, with only ≈ 3 additional events when a photon was detected in only one spatial mode, without coincidence. The developed theoretical model is in good qualitative and quantitative agreement with the experimental data for low m and is in good qualitative agreement for any value of m. We achieved significant improvements on separate parts of the source during the project. Putting them all together didn't happen within the timeline of the project due to various delays including covid but will be completed in the next few months. We are confident that the final combination of source+crystal+electronics+loop will be even more remarkable. We have also designed, and implemented an active switching setup and demonstrated excellent quality non-classical interference with it, which is crucial for future applications of the source. In addition, we presented a new application for this source of photons that uses passive many-mode linear networks to recreate quantum interference effects comparable to deterministic sources acting on fewer modes.

The next steps are to develop an 8-mode testbed of the full technology, en route to a large-scale Noisey Intermediate Scale Quantum (NISQ) machine. We propose a next-generation project, building on the success of this one and recent results in the literature [20], to develop the science and technology required to build a large-scale programmable NISQ machine in a US-Australia collaboration. Specifically, key steps involve:

- **Extending operation of our world-leading photonic-state sources to high squeezing levels, with active phase locking. The aim would be to have the worlds-best pulsed squeezed sources, a highly realistic goal based on the performance demonstrated here. These sources will enable operation of sampling-style NISQ protocols with less mode switching requirements;**

- **Hybridising our temporal mode switching technology with spatial mode switching technology, to optimise complexity-vs-loss payoff of the complicated programmable unitary mode transformations required to implement algorithms. We have two highly-promising spatial mode designs – one based on low-loss crystalline elements and one based on micro fabricated optical elements – and can investigate one or both of these paths, depending on funding. We have demonstrated technological and scientific experimental expertise in both;**
- **Scale-up of ultrahigh-efficiency detector arrays, including implementation of partially-number-resolving fast, high efficiency detectors, which will be a transformational advance for all of the quantum photonics field.**

References

[1] J. Preskill, arXiv e-prints, arXiv:1203.5813 (2012).

[2] A. P. Lund, A. Laing, S. Rahimi-Keshari, et al., Physical Review Letters **113**, 100502 (2014).

[3] M. Bentivegna, N. Spagnolo, C. Vitelli, et al., Science Advances **1**, e1400255 (2015).

[4] S. Aaronson and A. Arkhipov, in Proceedings of the forty-third annual acm symposium on theory of computing (2011), pp. 333–342.

[5] M. M. Weston, H. M. Chrzanowski, S. Wollmann, et al., Opt. Express **24**, 10869 (2016).

[6] E. Knill, R. Laflamme, and G. J. Milburn, Nature **409**, 46 (2001).

[7] S. Slussarenko and G. J. Pryde, Applied Physics Reviews **6**, 041303 (2019).

[8] L. Caspani, C. Xiong, B. J. Eggleton, et al., Light: Science & Applications **6**, e17100 (2017).

[9] J. J. Guanzon, A. P. Lund, and T. C. Ralph, Physical Review A **102**, 032606 (2020).

[10] C. K. Hong, Z. Y. Ou, and L. Mandel, Physical Review Letters **59**, 2044 (1987).

[11] S. L. V. Giovannetti and L. Maccone, Nature Photonics **5**, 222 (2011).

[12] K. R. Motes, J. P. Olson, E. J. Rabeaux, et al., Physical review letters **114**, 170802 (2015).

[13] J. P. Olson, K. R. Motes, P. M. Birchall, et al., Physical Review A **96**, 013810 (2017).

[14] M. Takeoka, K. P. Seshadreesan, C. You, et al., Physical Review A **96**, 052118 (2017).

[15] C. W. Helstrom and C. W. Helstrom, *Quantum detection and estimation theory*, Vol. 84 (Academic press New York, 1976).

[16] S. L. Braunstein and C. M. Caves, Physical Review Letters **72**, 3439 (1994).

[17] A. Dosseva, Ł. Cincio, and A. M. Brańczyk, Phys. Rev. A **93**, 013801 (2016).

[18] R. S. Bennink, Phys. Rev. A **81**, 053805 (2010).

[19] F. Graffitti, P. Barrow, M. Proietti, et al., Optica **5**, 514 (2018).

[20] H.-S. Z. et al., Science **370**, 1460 (2020).